ACS OMEGA

Open Access

http://pubs.acs.org/journal/acsodf

Article

Probing Relative Humidity Impact on Biological Protein Bovine Serum Albumin and Bovine Submaxillary Gland Mucin by Using Contact Resonance Atomic Force Microscopy

Erum Kakar,* Saira Riaz,† and Shahzad Naseem†

Cite This: *ACS Omega* 2023, 8, 32765−32774

Read Online

ACCESS | Metrics & More | Article Recommendations

ABSTRACT: In biomaterials, a substantial amount of research has been placed on the mechanical properties of biomolecules and their interactions with body fluids. Bovine serum albumin (BSA) is a widely studied model protein, while bovine submaxillary gland mucin (BSM) is another cow-derived protein frequently employed in research. Films were examined with contact resonance atomic force microscopy (CR-AFM), and the results showed that the mechanical characteristics of the films were affected by the relative humidity. We quantitatively analyze the viscoelasticity of these proteins after they have been subjected to humidity by measuring the resonance frequency and quality factor. The findings indicate that prolonged humidity exposure has a different effect on the mechanical properties of BSA and BSM films. The results show that after exposure to humidity, the resonance peaks of BSA shift to the left, indicating stiffness, while those of BSM shift to the right, indicating hydration. Moreover, BSM's hydration is caused by relative humidity, leading to a constant increase in resonance frequency and material softness. Contrarily, BSA showed a decrease in contact resonance frequency due to ongoing strain-induced deformation, indicating increased material stiffness. The findings have significance for the design and development of biomaterials for a variety of applications, such as the delivery of drugs, the engineering of tissue, and the development of biosensors. Our research demonstrates that CR-AFM has the potential to become a non-invasive and sensitive method that can be used to characterize the mechanical characteristics of biomolecules and their interactions with bodily fluids.

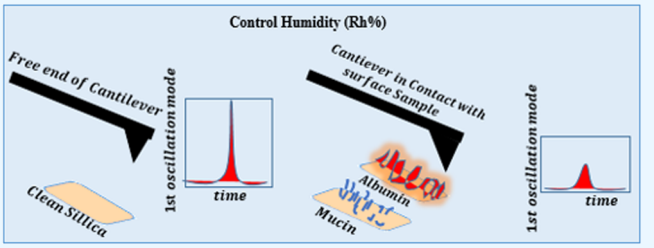

INTRODUCTION

Biocompatibility is the ability of a material to carry out a certain function while evoking the desired reaction from the host. The material's capacity to do this depends on how it interacts with body fluids and tissues.[1] As a result of their adsorption properties, biological proteins' shape and mechanical attributes become important. The successful implantation of prosthetic devices that come into touch with blood, fluids, and tissues depends on these bioproteins.[1] The mechanical characteristics of protein changes in film mechanics, resonance frequency, quality factor, and viscoelasticity tan(δ) under humidity fluctuations from RH 0% to RH 98% are examined in this work in two different types of films made of two biomolecules, bovine submaxillary mucin (BSM), derived from cows, and bovine serum albumin (BSA), a model protein used in a lot of research.[2] BSA protein has outstanding stability and amazing binding properties.[3−5] It is essential for transporting and delivering diverse compounds like ions,[6] surfactants, and pharmaceuticals.[7] It comprises a sizeable amount of plasma proteins, fatty acids, and metabolites.[8]

Mucins are extensive extracellular glycoproteins with sizes ranging from 0.5 to 20 MDa, with carbohydrates accounting for 69% of the mass fraction.[9] The shape and properties of mucus depend on the interaction between the sugar chains of the glycoprotein subunits.[9] Salts, lipids, proteins, and water comprise 95% of the mucus composition. However, the glycoprotein mucin is the primary component that imparts its viscoelastic properties.[10] In biological systems, mucins are commonly found as thin films encompassing moist tissues. Hydrating the mucin films instead of the bulk material is the primary method to prevent tissue dehydration. As a result, lubricated surfaces experience reduced friction.[11] The study suggests mucin coatings can prevent microbial infections on polymeric biomaterials.[12] Despite the significant differences in the adsorption characteristics of the two individual proteins (BSA and BSM), BSA produced a thin and rigid layer.[1,13] In contrast, BSM formed a thick and diffuse layer that was highly viscoelastic with varying relative humidity.[10,14] BSM was adsorbed on mica surfaces, creating soft and hydrated layers

Received: May 28, 2023
Accepted: August 15, 2023
Published: August 30, 2023

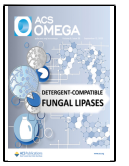

using the Surface Force Apparatus.[12] BSMs with a high BSA content exhibited increased stiffness and viscosity, leading to higher friction than the layers composed of purified BSM.[13]

The ability of mucin to break hydrogen bonds, unfurl, and partially denature was demonstrated by increasing the viscosity of pure mucin and mucin-albumin combinations.[15] The considerable rise in mucin viscosity brought on by serum proteins during synovial effusions may be to blame for the stiffness and increased burden of arthritic joints.[16] It is possible to simultaneously detect changes in the characteristics of proteins and the strength of each layer. There was no lateral diffusion in BSA.[17] A glass transition in mucins has been seen in investigations using the Quartz Crystal Microbalance[1,10] and calorimetric analysis,[18,19] at RH levels between 60 and 70%.[10,20,21] Juglone (JL), a powerful anticancer medication component, binds to more than 99.0% of serum albumin, indicating a high affinity for this protein.[22] When the RH of the air changes, the mucous gel's high water content causes a delayed alteration in water activity.

The mucous gel dries and loses water in dry environments.[14] This can happen in many diseases, such as cystic fibrosis,[23,24] asthma,[25] gastric cancer,[26] primary Sjogren's syndrome (PSS),[27] and rhinorrhea.[28] Mucin maintains the epithelium hydrated, prevents infections and hazardous toxins from accessing it, and acts as a porous gel layer for gas and nutritional exchange with the epithelium beneath.[9,29] According to studies, mucin can form liquid crystalline phases, and its phase behavior depends on how hydrated it is.[30] The primary objective of this research is to determine how the viscoelastic properties of BSA and BSM change as relative humidity (RH) increases.

The viscoelastic properties of materials are characterized by the storage modulus (E'), which measures the stored energy or elastic component, and the loss modulus (E''), which measures the dissipated energy or viscous component. The ratio of dissipated to stored energy is represented by the tangent of the phase angle, or $\tan(\delta)$, which is determined by the elastic and viscous responses. The material's contact resonance frequency (ω_n) and quality factor (Q_n) can be used to calculate $\tan(\delta)$.[31,32] The contact resonance atomic force microscopy (CR-AFM) method is often utilized to study the viscoelasticity of materials. The cantilever is excited by Brownian motion due to mechanical contact with the sample.[33,34]

This study takes advantage of the low-total-force contact resonance force microscopy (LTF-CRAFM) technique to investigate the viscoelastic properties of cellulose nanofibrils, which are stiff, nanoscale structures.[35] This study used Brownian motion excitation to minimize damage while measuring polyurethane (PU) samples with CR-AFM. Analysis of the shape of the resonance peak and the values of $\tan(\delta)$ revealed changes in the viscoelastic properties of PU films as the relative humidity increased.[36] By manipulating the Brownian motion of the cantilever, we demonstrate the feasibility of tracking the influence of relative humidity on the material's mechanical properties, as indicated by changes in the resonance frequency and quality factor. Specifically, we aim to investigate the hydration behavior of BSA and BSM at different relative humidity levels, a study that has not yet been conducted. Our research explores the mechanical responses of BSA and BSM under varying relative humidity levels, using cantilever oscillation damping as a measure of contact resonance frequency and quality factor. This study is the first attempt to understand how the level of humidity affects the way biomolecules behaves mechanically. It could have important implications for developing new biomaterials and biomedical devices.

EXPERIMENTAL SECTION

In this research, biological coatings derived from bovine submaxillary mucin (BSM) Type I-S, M3895, comprising bound sialic acid (Sigma Aldrich) with a molecular weight range of 0.4−4 MDa, and commercially available Bovine Serum Albumin (BSA) (A9056-10G) were procured from Sigma Aldrich. The sample preparations utilized BSA concentrations of 0.6 and 1.2 mg/mL (denoted as BSA06 and BSA12, respectively) and BSM concentrations of 0.6 and 1.2 mg/mL (referred to as BSM06 and BSM12, respectively). Solutions were prepared using ultrapure water (Milli-Q) (Millipore, Milli-Q Plus system). The hydrophilic silica-coated crystals were treated in accordance with a straightforward procedure to produce hydrophobic surfaces.[17] They were washed with Milli-Q water and ethanol, and then dried with nitrogen gas. Lastly, a plasma cleaner (Harrick Scientific Corp., model PDC-32 G, Ossining, NY) treated the surface using low-pressure (200−600 mtorr) residual air via a glow discharge unit for 10 min, which results in a water contact angle of results.[17]

Drop Casting. Drop casting was employed as a deposition technique for applying Bovine Serum Albumin (BSA) and bovine submaxillary mucin (BSM) onto a silica surface with a surface area of 100 mm^2. The silica surface was cleaned using the aforementioned method, after which 120 $\mu g/mm^2$ of BSA and BSM, along with 136 $\mu g/mm^2$ of albumin and mucin, were deposited on the sample surfaces using a micropipette. The corresponding masses of the silica surface for these concentrations were approximately 120 and 136 μg for BSA and 120 and 136 μg for BSM. The volume, representing the ratio between mass and density, was used to determine the thickness measurement by utilizing the formula for the ratio between volume and surface area. Consequently, the calculated thicknesses were found to be 1200 nm and 1360 nm, respectively.

Four samples were prepared using this procedure: BSA06, BSA12, BSM06, and BSM12 films. The BSA/BSM drop covers the entire surface; all calculations were performed for the entire surface area. The samples were placed in a desiccator with silica gel for 24 h to allow the evaporation of the solvent (T = 22 °C and RH = 30%).

Contact Thermal Noise AFM. In this AFM mode, we studied how RH affected the biological coatings' viscoelastic properties. Specifically, we employed a method that analyzes changes in the cantilever's Brownian motion as it interacts with the sample under investigation. This technique measures alterations in the cantilever's resonance frequency and quality factor, as depicted in Figure 1. Previous studies have also employed this method.[33,34,37]

A commercial atomic force microscope with a sealed liquid cell (MultiMode 8 SPM with a NanoScope V control unit; Bruker AXS, Santa Barbara, CA). RH was controlled by a flow rate of nitrogen at 2 bar through a setup GenRH (Surface Measurement System, Pragolab, Prague, Czech Republic) while entering the liquid cell with a sealed compartment where 10 units gradually increased RH on the GenRH- Software and particularly waiting for 10 min before the next 10 unit increment. A nominal cantilever of Olympus, Japan (OMCL-AC240TS); 2 N/m spring constant, length = 240 μm, and

https://doi.org/10.1021/acsomega.3c03740
ACS Omega 2023, 8, 32765−32774

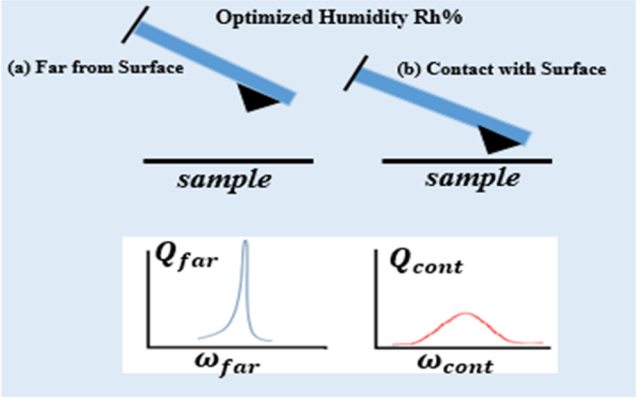

Figure 1. Measuring resonance frequency at the end of the cantilever when far from surface ω_{far} and quality factor Q_{far}, and the frequency in contact with sample ω_{cont} and Q_{cont} quality factor. (a) When the cantilever is far from a sample, no real damping is seen. (b) Cantilever near the surface; the quality factor goes down.

width = 40 μm was used for the measurements. Calibration in AFM is usually performed using "Force versus Z" (F vs Z). Curves F vs Z are initially in volts and cantilever vertical in nanometers (Z). The photodiode registers the cantilever's deflection in these curves when the tip-sample distance is lowered.[38] Sometimes, the tip and sample collide (contact point), and if we increase the force, the cantilever bends until some preselected maximum deflection (set point).[38,39] The curve region between the contact point and the maximum deflection is usually fitted to a straight line (while pressing the AFM tip against a hard sapphire surface estimated the photodetector signal slope).[36] The slope of this line has units V/nm. The inverse of this slope is the "deflection sensitivity". It lets us transform data taken in volts to nm (deflection is taken in volts by the photodiode, then with the deflection sensitivity, we can transform this deflection to nm, representing how much the cantilever has bent).[38] The deflection sensitivity of the cantilever was measured as 30 nm/V with a deflection set point (contact force) of 0.5 V, which indicates a threshold deflection of d = 15 nm, and the calculated static applied force F during the measurements was ~9 nN. In all experiments, the initial calibration is done with a thermal tune,[40] and the tip must be out of contact. At the same time, the sample data acquire the vibration of the cantilever, and the spectrum of the thermal noise should be first determined to calibrate the elastic constant. Thus, this spectrum measures the deflection (the normal force signal) across a specific frequency range. The data collected experimentally at a certain frequency and the power spectral density (PSD) are then computed. For a damped harmonic oscillator with a resonance frequency, the PSD equation near the resonance frequency is given by eq 1.[40] The spectral noise measurement of the cantilever movement is fitted to the Lorentzian function for analyzing the spring constant.[40−42]

$$|f(\omega)| = \sqrt{\frac{\alpha_{th}}{\left[1 - \left(\frac{\omega}{\omega_0}\right)^2\right]^2 + \left[\frac{\omega}{(\omega_0 Q)}\right]^2}} + n_{tec}^0 \quad (1)$$

The second step for the calibration is Sader et al. method. Sader's method depends on the hydrodynamic properties of the cantilever and the fluid in which it is submerged.[43,44] The cantilever's width and length are the determining factors for elastic constant (these are the source of error in this method). However, the thermal noise spectrum should be first determined to calibrate the elastic constant. This method is independent of the thickness of the cantilever.[44]

Experimental Protocol. The initial step involved exposing the sample to a nitrogen flow for 10 minutes in the sealed compartment of the Gen-RH setup. Next, the thermal noise spectra for the free lever were measured at a specific value of relative humidity (RH). A complete humidity ramp from 0 to 98% RH in the adsorption direction was conducted, and the thermal noise spectra for the specific value of 0−98% RH in the adsorption direction were measured with the tip and sample in contact. The contact resonance was verified to be approximately equal to the expected value of the free resonance *4.37. The measurements were performed at a fixed point, and the AFM tips were plasma cleaned using a glow discharge machine (PDC-32 G, Harrick Scientific Corp., Ossining, NY) at low pressure and residual air for 5 minutes between each set of experiments. Only one cantilever was used to collect the contact resonance data with a supported and unsupported cantilever. The first resonance peak from the PSD of the non-supported and supported cantilever was fitted as the Lorentz function to estimate the frequency and quality factor.[36,45,46] The mean and standard deviation values of frequencies and quality factors were calculated, and error bars were plotted for 40 spectra. MATLAB was used for processing the spectra, with the PSD generated via the Periodogram as the initial step. The Periodogram is a data analysis technique that examines a frequency-domain model of an equispaced time series.[47]

Theoretical Analysis of Contact Resonance-AFM. According to an Equipartition Theorem, every mode of vibration does have a mean thermal energy equal to k_BT, $\frac{1}{2k_BT}$ in terms of its potential energy or $\frac{1}{2k_BT}$ for the kinetic energy,[48] where k is the Boltzmann constant and T is the temperature of the cantilever. One must first determine the flexural vibration amplitudes for its cantilever to determine the vibration energy before we can get the overall thermal deflection amplitude. This is accomplished by modeling the rectangular cantilever utilized for AFM with an Euler−Bernoulli beam in which an equation controlled flexural vibrations.[46,48,49]

$$EI\frac{\partial^4 y}{\partial x^4} + \rho AL^2\frac{\partial^2 y}{\partial t^2} = 0 \quad (2)$$

where $y(x, t)$ is the upward deflection of the cantilever with longitudinal direction. $y(x, t)$ can be split into their temporal and spatial contributions; therefore,[36,48] $y(x, t) = y(x)\cos(\omega t + \delta)$, where $K^4 = \frac{\rho A\omega^2}{EI}$, and eq 2 is the differential equation for spatial contribution, as the temporal contribution can be solved as a cosine function. The general solution should combine all functions that, after four differentiation, remain the same except for q. Normalize the coordinate y (along the length of the cantilever), so it can only take values between 0 and 1, so new variable $\zeta = x/L$ (L, length of the cantilever) where $q = KL$

$$y(\zeta) = S_1\cos(K\zeta L) + S_2\sin(K\zeta L) + S_3\cosh(K\zeta L) + S_4\sinh(K\zeta L) \quad (3)$$

https://doi.org/10.1021/acsomega.3c03740
ACS Omega 2023, 8, 32765−32774

Equation 3[49] can all be calculated for every combination of boundary conditions, which support a variety of possible cantilever situations at the beam end where the first three of the beam boundary conditions are similar. The fourth boundary condition should be supplied to find the flexural modes for[36,40] free cantilever

$$1 + \cos(q)\cosh(q) = 0 \tag{4}$$

The result of numerically resolving this equation is[48] q_n = 1.88··· (n = 1, ···), which are the first wavenumber for the free non-supported cantilever from equation.[48] In the case of the supported cantilever, the fourth boundary condition is

$$\sin(q)\cosh(q) - \cos(q)\sinh(q) = 0 \tag{5}$$

When the above equation is numerically solved, q_n = 3.93··· (n = 1, ···). The fourth boundary condition should account for the transition from the free, unsupported cantilever to the supported cantilever. The forces exerted on a cantilever's unsupported end cause a corresponding amount of deflection at the free end.[36,50] AFM cantilever contact mechanically with the viscoelastic surface; this relation is modeled as the Kelvin–Voigt model.[51] According to the model, the contact with the free arm of the lever and the sample mainly comprises the spring (a conservative part) plus the dissipative part (a dashpot).[36,52]

A dashpot represents sample dissipation χ, and a spring K_* represents sample rigidity, as shown in Figure 2. Sample stiffness affects the contact resonance, while sample dissipation affects the contact resonance's quality factor at constant stiffness.

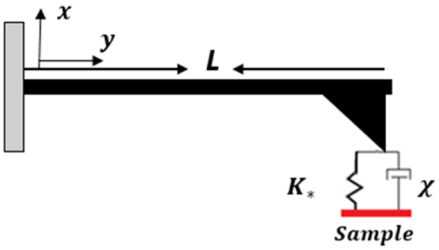

Figure 2. Tip-sample forces of a viscous frequency elastic sample having AFM contact with the tip are simulated using a linear spring-dashpot system.

The wavenumber is the complex number $\acute{q}_n$ (for each flexural). The characteristic used for flexural vibration becomes[36,48,50,53]

$$\cos(\acute{q}_n)\sinh(\acute{q}_n) - \sin(\acute{q}_n)\cosh(\acute{q}_n) = \frac{\acute{q}_n^{\,3}}{3\left(\frac{k_*}{k_c} + i\chi\frac{\omega_n}{k_c}\right)}[1 + \cos(\acute{q}_n)\cosh(\acute{q}_n)] \tag{6}$$

Equation 6[46,50,54] defines the complex wavenumber $\acute{q}_n = a_n + ib_n$ where the real part in vibration mode is associated with the frequency $a_n = \left(\frac{\omega_n}{\omega_f}\right)^{1/2} k_f$ and the complex wavenumber's imaginary component relates to energy loss known as dissipation.

Equation 6 allows for the calculation of the complex wavenumber $\acute{q}_n = a_n + ib_n$. The real part of the complex wavenumber is related to the frequency of the vibration mode. Where the dissipation is associated with the imaginary portion of the complex wavenumber. From eq 6 damping factor χ_n represents the complex components at an eigenmode frequency ($\omega = \omega_n$) is $\chi_n = \chi_f + \frac{4\omega_n b_n}{a_n}$, defines viscoelastic dissipation contact with a higher value of χ_f this dissipation is from free fundamental eigenmode in air.[36] If the cantilever contacts with the viscoelastic sample, then the initial complex wavenumber is computed using the relation of a_n, b_n, and $\chi_n = \frac{\omega_n}{Q_n}$.[33,36,37,42]

$$\acute{q}_n = \left(\frac{\omega_n}{\omega_f}\right)^{1/2} q_f \cdot \left[1 + i\left(\frac{1}{4Q_n} - \frac{\omega_f}{4\omega_n Q_f}\right)\right] \tag{7}$$

To estimate both normalized tip-sample contact toughness α and dampening coefficient β, calculations are performed using the real and imaginary components.[36,45]

$$\theta + i\beta(\acute{q}_n^{\,2}) = \frac{\acute{q}_n^{\,3}[1 + \cos(\acute{q}_n)\cosh(\acute{q}_n)]/3}{\cos(\acute{q}_n)\sinh(\acute{q}_n) - \sin(\acute{q}_n)\cosh(\acute{q}_n)} \tag{8}$$

Using eq 8,[36,45] the sample's storage and loss moduli can be determined. Also of note is the fact that CR-AFM viscoelastic characterization does not need precise details, such as tip geometry, about the tip-sample area of contact.[31] CR-AFM quantifies the sample's viscoelasticity in light of their loss tangent.[36,55]

$$\tan\delta_n = \frac{\omega_n\chi}{k_*} \tag{9}$$

Using the fundamental mode, the loss tangent was estimated, and we derived the interacting elastic constant α and the damping coefficient β. Using these coefficients, the loss tangent of the sample was estimated and the above equation could be rewritten.[37,42,52]

$$\tan\delta_n = q_f^{\,2}\frac{\beta\omega_n}{\theta\omega_f} \tag{10}$$

It is verified that by experimentally measuring ω_f, Q_f, ω_n, it is possible to find tan δ_n. These contact and free values were used in the protocol of the MATLAB code where the first wavenumber for the free non-supported cantilever from (eq 4) q = 1.88 is used. The two components of the initial complex wavenumber that are real and imaginary are calculated from (eq 7). Now, calculations being made to derive that complex wavenumber from the real as well as imaginary components by $\acute{q}_n = a_n + ib_n$, this is used in the right-hand side of (eq 8) from which the values of β and θ are calculated. Eventually, the loss tangent is calculated as in (eq 10) from the q, β, θ, ω_n, ω_f.[36]

RESULTS AND DISCUSSION

For free non-supported cantilever, the first resonance peaks are detected at RH% varying from 0 to 98 RH%, shown in Figure 3. The first flexural eigenmode peaks for the free non-supported cantilever were unaffected by RH%, which indicates that this environmental parameter RH% induced water adsorption had no significant effect on the freestanding cantilever. The change in humidity from RH 0% to RH 20% allowed the resonance peaks at higher frequencies to be narrower resonance peaks for protein films.

The relative humidity (RH%) significantly impacted the resonance peaks of protein films. Initially, the resonance peaks

https://doi.org/10.1021/acsomega.3c03740
ACS Omega 2023, 8, 32765−32774

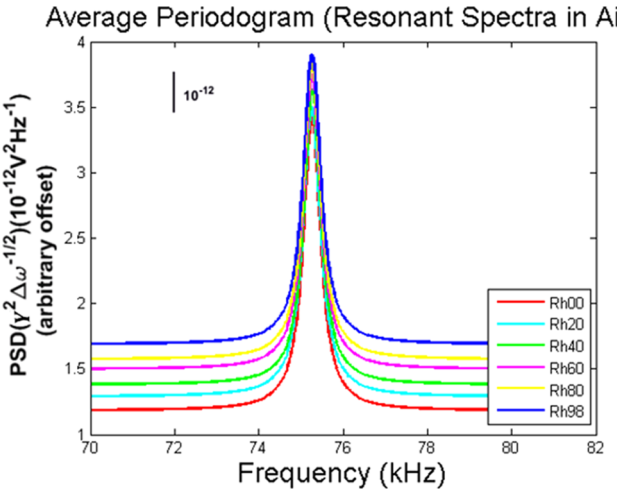

Figure 3. Thermal noise signal for a freestanding cantilever (unaffected by environmental factors).

for protein films with RH% 0 were centered and fell in lower frequency ranges. As the RH% increased from 20 to 98% RH, the resonance peaks became more spread.

Nonetheless, as the RH% increased from RH 20% to RH 98%, the resonance frequencies changed, and the peaks became more spread out. Figures 4a,b and 5a,b clearly show a shift in the resonance peaks for BSA and BSM, respectively.

Figure 4a,b illustrates a shift in the resonance peaks for (BSA) at lower humidities, specifically RH 0%, where the peaks appeared at lower frequencies. With increasing humidity (i.e., RH 20%, RH 40%, and RH 60%), both BSA sample peaks increase vibrational frequencies smoothly toward the left side of the axis. At higher humidities (i.e., RH 80% and RH 98%), the peaks shifted further to the left, as shown in Figure 4a,b. This peak shift indicates that BSA adopts a flat, rigid conformation at the lowest and highest humidity ranges. The observed peak trend was confirmed for both BSA06 and BSA12 thicknesses. The QCM-D experiment validated the behavior of BSA, which was extracted from commercial mucin BSM fractionation using an anion exchange step.

The introduction of BSA did not induce any change in frequency, indicating that BSA acts as a barrier to prevent BSM adsorption.[1] This research further supports the role of BSA as a blocking agent in the biochemical analysis of BSA, serving as an initial step to hinder the nonspecific adsorption of antibodies and other biomolecules.[56,57] In analyzing the data provided in Figure 5a,b, it is evident that the behaviour of BSM (backscattering magnitude) has been impacted by deviations in relative humidity (RH). Particularly since tracking the RH range from RH0% to RH20%, which appears to have an apparent centralised control of the RH dependence. When RH rises, an even and consistent increase in frequencies becomes apparent throughout the humidity interval of RH 30% to RH 98%. The boost in frequencies is followed by the appearance of broader peaks that incrementally shift forward towards the higher RH values across the axis.

BSM is a glycoprotein that is water-adsorbent, with a carbohydrate content of approximately 61−69 wt % in comparison to other mucins.[14,58,59] BSM's carbohydrate side chains interact primarily with water molecules.[14] Studies have demonstrated that proteins absorb less water than carbohydrates. However, at relative humidity rates exceeding 77%, BSM absorbs considerable water due to electrostatic repulsive interactions between carbohydrate side chains.[14,59] Sialic acid accounts for approximately 32−36 wt % of BSM, a significantly greater percentage. The sialic acid sections contribute to a negative charge on the mucin molecule, attracting polar water molecules.[58−60] As the electrostatic repulsive forces of BSM remain greater, its sorption capacity is enhanced at higher relative humidity levels (RH77%). The QCM-D technique was used to measure the water-stimulated isothermal glass transition for mucin coatings. The glass transition can occur at equivalent humidity levels of RH 60%−RH 80%, as determined by sorption calorimetric measurements.[14]

The shifts in peak positions exhibit a comparable increment in both thicknesses with an increase in humidity, particularly at higher relative humidity levels of Rh 80% and Rh 98%. The augmented stiffness of albumin BSA at higher humidity is not attributed to capillary condensation but rather the intrinsic stiffness of the sample.[61] To investigate whether the RH-dependent capillary forces between the AFM tips and samples affect the contact resonance measurements, previous studies have been conducted.[36,61,62] As depicted in Figure 6a, the decrease in resonance frequencies provides evidence for changes in damping from the BSA, which further supports the rigidity of the sample.

The surfaces are known to stiffen due to capillary condensation, which causes an increase in contact resonance

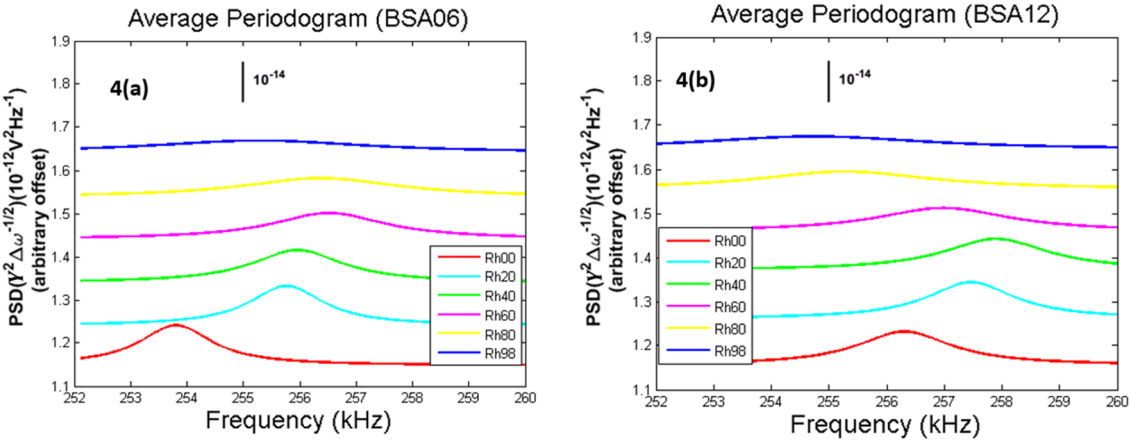

Figure 4. Thermal resonance signals of a cantilever in mechanical contact with (a) BSA06 and (b) BSA12 coatings at various RH% levels.

https://doi.org/10.1021/acsomega.3c03740
ACS Omega 2023, 8, 32765−32774

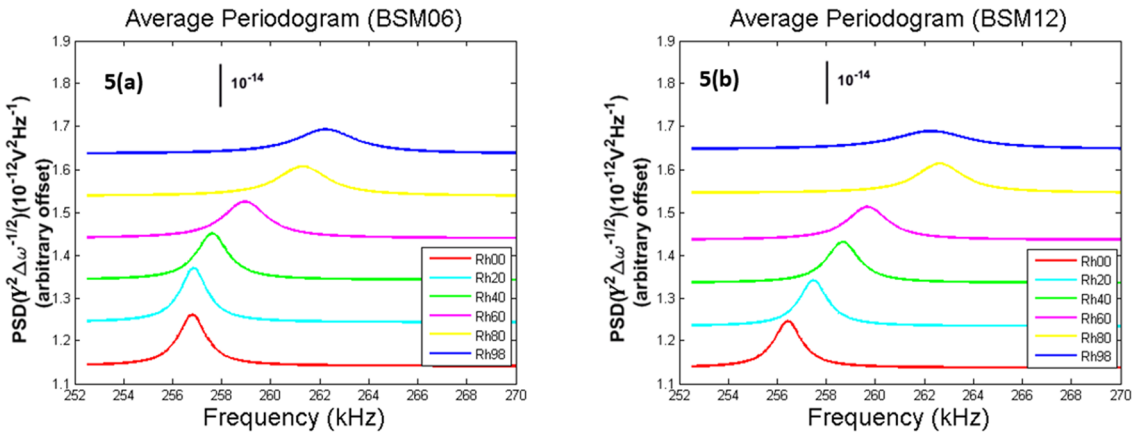

Figure 5. Recorded thermal spectrum for the bovine submaxillary mucin gland cantilever for two thicknesses: (a) BSM06 and (b) BSM12.

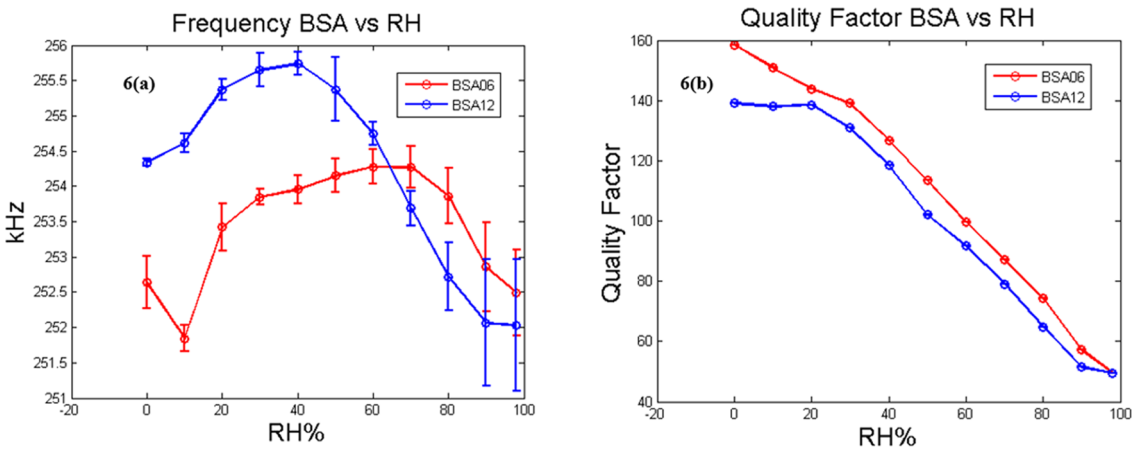

Figure 6. (a) Contact resonance frequency values and (b) the related Quality Factor values for BSA06 and BSA12.

frequencies.[36,61] However, the opposite effect is observed in Figure 6a for BSA, where lower contact frequencies are seen in both initial and higher RH ranges.[54]

In order to confirm whether the observed variations in quality factors are related to sample damping and not modal damping of the cantilever, the loss tangent for BSA with bare silica substrate as a control is calculated. The rigid substrates are not expected to exhibit real damping variation. As shown in (Figure 7), sample damping is from the proteins.[54]

The loss tangent (δ) damping is calculated from viscoelasticity/elasticity ratios, i.e., tan(δ) trend with a bare silica surface from BSA06 and BSA12. It is important to determine whether the increase of loss tangent with RH is actually from BSA or is due to the adsorption of thin water films onto surfaces. Under ambient circumstances, a water neck forms around the AFM tip and substrate, and the hydrophobicity between both tip and sample, in addition to the surrounding humidity, determines the attractive contact.[38]

Capillary condensation increases adhesion forces and the surface's effectiveness of hardening.[61] These capillary forces will increase the total contact force and thereby increase the measured in-contact natural frequency of the system.

However, the decline in BSA contact resonance frequency values is justified by the observed data. The decline in resonance frequency leads to lower oscillation amplitude.[63] It would be of high interest to study viscoelastic creep.

Viscoelastic creep implies the time-dependent deformation responses of a material when exposed to applied stress.[64] When

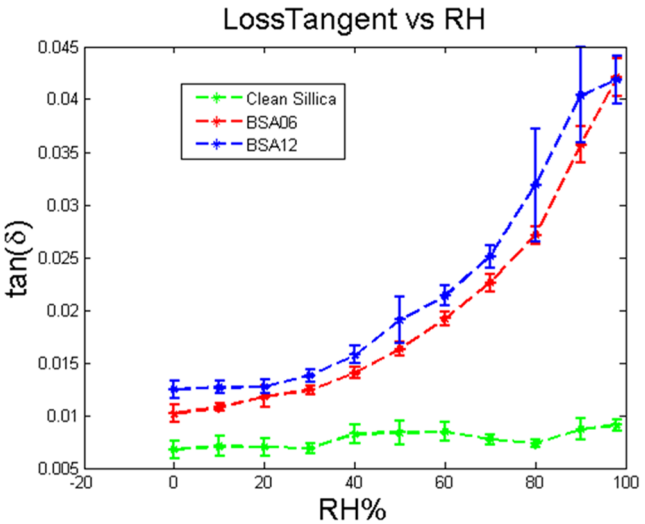

Figure 7. Loss tangent (tan δ) from BSA both thickness of BSA06 and BSA12 with damping comparison to the bare silica surface.

a viscoelastic material experiences creep, as apparent from the experimental results in Figure 6a, the contact resonance frequency demonstrates a steady decline over time the material receives deformation under constant strain, consequently impacting the quality factor Figure 6b through a decrease. The creep deformation is evident from the loss tangent

https://doi.org/10.1021/acsomega.3c03740
ACS Omega 2023, 8, 32765−32774

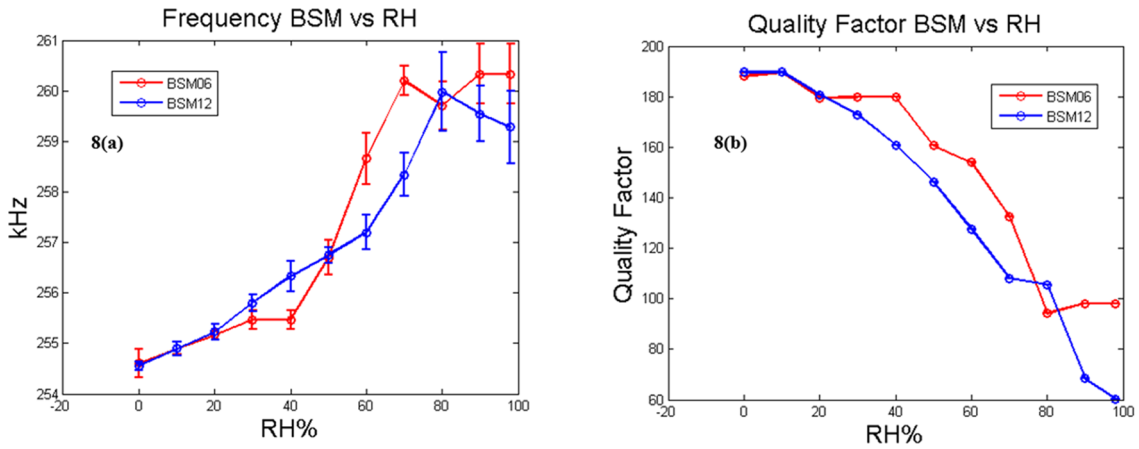

Figure 8. (a) Contact resonance frequencies of BSM06 and BSM12 and (b) the corresponding quality factors.

increase in force−displacement ratio in Figure 7, supporting the stiffening behavior for BSA.[36]

The resonance frequencies of BSM06 and BSM12 increased with an increasing RH, as illustrated in Figure 8a. At lower humidity levels (Rh 0%−Rh 20%), the quality factor increased, resulting in a relative reduction in the loss factor (tan δ). The higher quality factor in Figure 8b refers to lightly damped oscillations at initial RH, whereas the low-quality factor at higher RH refers to heavily damped oscillations.[54] However, both coatings were observed to exhibit RH dependence throughout the observed range, indicating that they essentially had comparable quantities of RH dependence in the 20−98% RH range. When the RH was raised from 0 to 20% in bioprotein coatings, tan(δ) remained largely unaffected as shown in Figure 9, but it did increase when the RH was

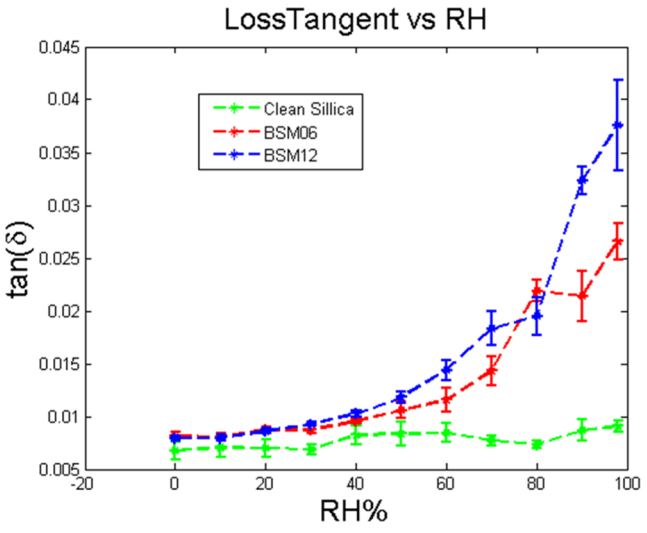

Figure 9. Comparing the Loss Tangent (tan δ) values as a substrate control with clean silica surface compared to thickness of both BSM06 and BSM12.

ramped up from 20 to 98%. The AFM mechanical response of the cantilever and the measured dependency of the loss tangent on RH were then examined to determine whether the RH effect was caused by the change in humidity or the AFM cantilever. In Figure 3, it is evident that RH does not affect the resonances of the cantilever when it is entirely free and unsupported.

This finding hints that RH-triggered moisture absorption on the cantilever did not significantly impact the reported statistics. It is also crucial to discuss how RH-induced changes in air viscosity affect the damping forces experienced by the cantilever's body when the tip and sample are in contact mode.[36] As RH increases, the air loses density and viscosity, resulting in a reduction in damping forces exerted on the cantilever.[65]

In our study, we observed the opposite effect in the humidity range of 20−98% RH, where higher RH levels caused greater damping of cantilever oscillations. This effect is attributed to the dominance of RH's impact on the sample's viscoelasticity over the cantilever itself. The variation in air viscosity between 0 and 20% RH can be neglected at ambient temperature.

The sample standard deviations derived from 40 registered spectra are shown for each humidity value. There are several uncertainties for each RH% value.

At ambient temperature, variation for air viscosity in the initial RH range between (0−20RH%) may be disregarded.[36,65] Thus, the impact of cantilever viscous damping on the claimed RH dependence of coating mechanical properties can be disregarded. It is worth noting that RH-dependent capillary forces lead to an increase in contact stiffness between the tip and the sample, resulting in higher contact resonance frequencies.[61] The role of viscous forces in the tip-sample interaction at high-frequency regions is crucial, as highlighted in prior research.[66]

Table 1 provides evidence of a reversal in the case of BSA at higher RH values. It is observed that in the high RH range (greater than Rh80%), the tangent loss values of BSA increased more significantly than those of BSM, possibly due to the action of BSA in preventing hydropsy. BSM, on the other hand, showed a decrease in damping factor with a mass-based hydration shift (from RH 0% to RH 98%) that is consistent across the BSM06 and BSM12 samples. The validity of the technique is supported by Figure 5a,b, which demonstrates the RH-induced hydration change in parallel.

CONCLUSIONS

Contact resonance atomic force microscopy (CR-AFM) made it possible to accurately measure the viscoelastic properties of materials with sizes on the micro- and nanoscale. The main objective of this investigation revolved around exploring how humidity affects the viscoelastic properties of BSA and BSM coatings.

https://doi.org/10.1021/acsomega.3c03740
ACS Omega 2023, 8, 32765−32774

Table 1. tan(δ) Values for BSA and BSM Computed from Contact Thermal Noise Spectrum, with Mean and Standard Deviation

	tan(δ) (10^{-2})					
	0%Rh	20%Rh	40%Rh	60%Rh	80%Rh	98%Rh
BSA06	1.01 ± 0.2	1.25 ± 0.1	1.32 ± 0.5	1.77 ± 0.6	2.48 ± 1.4	3.89 ± 1.8
BSA12	1.25 ± 0.8	1.27 ± 0.5	1.47 ± 0.6	2.02 ± 0.2	2.85 ± 4.5	4.11 ± 2.3
BSM06	0.81 ± 0.8	0.83 ± 0.5	0.91 ± 0.6	1.11 ± 0.2	1.81 ± 0.1	2.40 ± 0.4
BSM12	0.79 ± 0.2	0.83 ± 0.2	0.98 ± 0.2	1.33 ± 0.1	1.89 ± 0.5	3.42 ± 1.5

BSM exhibited unique hydration behavior due to its stronger attraction for water, while BSA consistently repelled water. The CR-AFM technique's accuracy was achieved by observing changes in the vibrational frequency and quality factor for both BSA and BSM coatings, instilling confidence in its capacity to characterize viscoelastic properties effectively. Notably, the hydration of BSM was significantly influenced by humidity levels, signifying the sensitivity of CR-AFM in understanding material responses to relative humidity. The drop in the contact resonance frequency of BSA is attributed to its deformation under continuous strain indicating material stiffness.

Overall, this study demonstrates the significant potential of CR-AFM as an effective tool for precisely characterizing material viscoelasticity, particularly in the context of relative humidity. Its application extends to diverse fields, encompassing materials science, biotechnology, and more, revealing exciting possibilities for further study.

AUTHOR INFORMATION

Corresponding Author

Erum Kakar − *COE in Solid State Physics, University of the Punjab, QAC, Lahore 54590, Pakistan;* orcid.org/0000-0001-8085-1697; Phone: +92 (0)318-4417485; Email: erum.kakar2@gmail.com

Authors

Saira Riaz − *COE in Solid State Physics, University of the Punjab, QAC, Lahore 54590, Pakistan*

Shahzad Naseem − *COE in Solid State Physics, University of the Punjab, QAC, Lahore 54590, Pakistan*

Complete contact information is available at: https://pubs.acs.org/10.1021/acsomega.3c03740

Author Contributions

†S.R. and S.N. contributed equally. The manuscript was written through the contributions of all authors. All authors have given approval to the final version of the manuscript.

Notes

The authors declare no competing financial interest.

ACKNOWLEDGMENTS

This work was done under the supervision of Dr. Javier Sotres Prieto and Dr. Juan Francisco Gonzalez-Martinez. The authors thank the Biomedical Science Department and Biofilms Research Center for Biointerfaces, Malmö University, Sweden, for providing space and research facility.

ABBREVIATIONS

AFM, atomic force microscopy; CR, contact resonance; BSA, bovine serum albumin; BSM, mucin from bovine submaxillary glands; RH, relative humidity

REFERENCES

(1) Feiler, A. A.; Sahlholm, A.; Sandberg, T.; Caldwell, K. D. Adsorption and Viscoelastic Properties of Fractionated Mucin (BSM) and Bovine Serum Albumin (BSA) Studied with Quartz Crystal Microbalance (QCM-D). *J. Colloid Interface Sci.* **2007**, *315*, 475−481.

(2) Kopac, T.; Bozgeyik, K.; Yener, J. Effect of pH and temperature on the adsorption of bovine serum albumin onto titanium dioxide. *Colloids Surf., A* **2008**, *322*, 19−28.

(3) Phan, H. T. M.; Bartelt-Hunt, S.; Rodenhausen, K. B.; Schubert, M.; Bartz, J. C. Investigation of Bovine Serum Albumin (BSA) Attachment onto Self-Assembled Monolayers (SAMs) Using Combinatorial Quartz Crystal Microbalance with Dissipation (QCM-D) and Spectroscopic Ellipsometry (SE). *PLoS One* **2015**, *10*, No. e0141282.

(4) Alkan, M.; Demirbaş, Ö.; Doğan, M.; Arslan, O. Surface properties of bovine serum albumin−adsorbed oxides: Adsorption, adsorption kinetics and electrokinetic properties. *Microporous Mesoporous Mater.* **2006**, *96*, 331−340.

(5) Sun, S.; Yue, Y.; Huang, X.; Meng, D. Protein adsorption on blood-contact membranes. *J. Membr. Sci.* **2003**, *222*, 3−18.

(6) Servagent-Noinville, S.; Revault, M.; Quiquampoix, H.; Baron, M.-H. Conformational changes of bovine serum albumin induced by adsorption on different clay surfaces: FTIR analysis. *J. Colloid Interface Sci.* **2000**, *221*, 273−283.

(7) Oliva, F. Y.; Avalle, L. B.; Cámara, O. R.; De Pauli, C. P. Adsorption of human serum albumin (HSA) onto colloidal TiO2 particles, Part I. *J. Colloid Interface Sci.* **2003**, *261*, 299−311.

(8) Spada, A.; Emami, J.; Tuszynski, J. A.; Lavasanifar, A. The Uniqueness of Albumin as a Carrier in Nanodrug Delivery. *Mol. Pharm.* **2021**, *18*, 1862−1894.

(9) Bansil, R.; Turner, B. S. Mucin structure, aggregation, physiological functions and biomedical applications. *Curr. Opin. Colloid Interface Sci.* **2006**, *11*, 164−170.

(10) Znamenskaya, Y.; Sotres, J.; Gavryushov, S.; Engblom, J.; Arnebrant, T.; Kocherbitov, V. Water Sorption and Glass Transition of Pig Gastric Mucin Studied by QCM-D. *J. Phys. Chem. B* **2013**, *117*, 2554−2563.

(11) Yakubov, G. E.; McColl, J.; Bongaerts, J. H.; Ramsden, J. J. Viscous Boundary Lubrication of Hydrophobic Surfaces by Mucin. *Langmuir* **2009**, *25*, 2313−2321.

(12) Lundin, M.; Sandberg, T.; Caldwell, K. D.; Blomberg, E. Comparison of the Adsorption Kinetics and Surface Arrangement of "as received" and Purified Bovine Submaxillary Gland Mucin (BSM) on Hydrophilic Surfaces. *J. Colloid Interface Sci.* **2009**, *336*, 30−39.

(13) Nikogeorgos, N.; Madsen, J. B.; Lee, S. Influence of Impurities and Contact Scale on the Lubricating Properties of Bovine Submaxillary Mucin (BSM) Films on a Hydrophobic Surface. *Colloids Surf., B* **2014**, *122*, 760−766.

(14) Znamenskaya, Y.; Sotres, J.; Engblom, J.; Arnebrant, T.; Kocherbitov, V. Effect of Hydration on Structural and Thermodynamic Properties of Pig Gastric and Bovine Submaxillary Gland Mucins. *J. Phys. Chem. B* **2012**, *116*, 5047−5055.

(15) List, S. J.; Findlay, B. P.; Forstner, G. G.; Forstner, J. F. Enhancement of the viscosity of Mucin by Serum Albumin. *Biochem. J.* **1978**, *175*, 565−571.

(16) Fraser, J. R.; Foo, W. K.; Maritz, J. Viscous Interactions of Hyaluronic Acid with Some Proteins and Neutral Saccharides. *Ann. Rheum. Dis.* **1972**, *31*, 513.

https://doi.org/10.1021/acsomega.3c03740
ACS Omega 2023, 8, 32765−32774

(17) Sotres, J.; Barrantes, A.; Arnebrant, T. Friction Force Spectroscopy as a Tool to Study the Strength and Lateral Diffusion of Protein Layers. *Langmuir* **2011**, *27*, 9439−9448.
(18) Davies, J. M.; Viney, C. Water−Mucin Phases: Conditions for Mucus Liquid Crystallinity. *Thermochim. Acta* **1998**, *315*, 39−49.
(19) Momoh, M.; Adikwu, M.; Ibezim, C.; Ofokansi, K.; Attama, A. Thermal characterisation of PEGylated Mucin. *Asian Pac. J. Trop. Med.* **2010**, *3*, 458−460.
(20) Strous, G. J.; Dekker, J. Mucin-Type Glycoproteins. *Crit. Rev. Biochem. Mol. Biol.* **1992**, *27*, 57−92.
(21) Madsen, J. B.; Sotres, J.; Pakkanen, K. I.; Efler, P.; Svensson, B.; Abou Hachem, M.; Arnebrant, T.; Lee, S. Structural and Mechanical Properties of Thin Films of Bovine Submaxillary Mucin Versus Porcine Gastric Mucin on a Hydrophobic Surface in Aqueous Solutions. *Langmuir* **2016**, *32*, 9687−9696.
(22) Zhao, P.; Gao, G.; Zhang, L.; Cai, Q.; Lu, N.; Cheng, L.; Li, S.; Hou, X. Drug-Protein Binding Mechanism of Juglone for Early Pharmacokinetic Profiling: Insights from Ultrafiltration, Multi-Spectroscopic and Molecular Docking Methods. *J. Pharm. Biomed. Anal.* **2017**, *141*, 262−269.
(23) Ratjen, F. A. Cystic Fibrosis: Pathogenesis and Future Treatment Strategies. *Respir. Care* **2009**, *54*, 595−602.
(24) Oliver, A.; Canton, R.; Campo, P.; Baquero, F.; Blazquez. High Frequency of Hypermutable Pseudomonas Aeruginosa in Cystic Fibrosis Lung Infection. *Science.* **2000**, *288*, 1251−1253.
(25) Thornton, D. J.; Rousseau, K.; McGuckin, M. A. Structure and Function of the Polymeric Mucins in Airways Mucus. *Annu. Rev. Physiol.* **2008**, *70*, 459−486.
(26) Bae, H. I.; Le, Y. H.; Na, Y. K.; Jung, Y. W.; Lee, S. M.; Yang, J. S.; Kim, D. S. Overexpression of D the MUC2 Gene Through Promoter Hypomethylation in Mucinous Cell Carcinomas and Signet Ring Cell Carcinomas of Gastric Cancer. *Genes Genomics* **2010**, *32*, 429−435.
(27) Amft, N.; Bowman, S. J. Chemokines and Cell Trafficking in Sjögren's Syndrome. *Scand. J. Immunol.* **2001**, *54*, 62−69.
(28) Sarin, S.; Undem, B.; Sanico, A.; Togias, A. The role of the nervous system in rhinitis. *J. Allergy Clin. Immunol.* **2006**, *118*, 999−1014.
(29) Neutra, M.; O'Malley, L.; Specian, R. Regulation of intestinal goblet cell secretion. II. A survey of potential secretagogues. *Am. J. Physiol.: Gastrointest. Liver Physiol.* **1982**, *242*, G380−G387.
(30) Viney, C. Mucus Liquid Crystallinity: is Function Related to Microstructural Domain Size? *Biorheology* **1999**, *36*, 319−323.
(31) Killgore, J. P.; DelRio, F. W. Contact Resonance Force Microscopy for Viscoelastic Property Measurements: From Fundamentals to State-of-the-Art Applications. *Macromolecules* **2018**, *51*, 6977−6996.
(32) Hurley, D. C.; Killgore, J. P. Dynamic Contact AFM Methods for Nanomechanical Properties. In *Scanning Probe Microscopy in Industrial Applications*; Yablon, D. G., Ed.; Nanomechanical Characterization; Wiley, 2013; pp 115−149.
(33) Tung, R. C.; Killgore, J. P.; Hurley, D. C. Liquid Contact Resonance Atomic Force Microscopy via Experimental Reconstruction of the Hydrodynamic Function. *J. Appl. Phys.* **2014**, *115*, No. 224904.
(34) Yao, A.; Kobayashi, K.; Nosaka, S.; Kimura, K.; Yamada, H. Visualization of Au Nanoparticles Buried in a Polymer Matrix by Scanning Thermal Noise Microscopy. *Sci. Rep.* **2017**, *7*, No. 42718.
(35) Hess, K. M.; K Jason, P.; Ashutosh, M.; S Wil, V. Viscoelastic-Mapping of Cellulose Nanofibrils Using Low-Total-Force Contact Resonance Force Microscopy (LTF-CRFM). *Cellulose* **2022**, *29*, 5493−5509.
(36) Gonzalez-Martinez, J. F.; Kakar, E.; Erkselius, S.; Rehnberg, N.; Sotres, J. Effect of Relative Humidity on the Viscoelasticity of Thin Organic Films Studied by Contact Thermal Noise AFM. *Langmuir* **2019**, *35*, 6015−6023.
(37) Tung, R. C.; Killgore, J. P.; Hurley, D. C. Hydrodynamic Corrections to Contact Resonance Atomic Force Microscopy Measurements of Viscoelastic Loss Tangent. *Rev. Sci. Instrum.* **2013**, *84*, No. 073703.
(38) Butt, H.-J.; Cappella, B.; Kappl, M. Force Measurements with the Atomic Force Microscope: Technique, Interpretation and Applications. *Surf. Sci. Rep.* **2005**, *59*, 1−152.
(39) Voigtländer, B. *Scanning Probe Microscopy: Atomic Force Microscopy and Scanning Tunneling Microscopy*; Springer, 2015.
(40) Butt, H. -J.; Jaschke, M. Calculation of Thermal Noise in Atomic Force Microscopy. *Nanotechnology* **1995**, *6*, 1−7.
(41) Hutter, J. L.; Bechhoefer, J. Calibration of Atomic-Force Microscope Tips. *Rev. Sci. Instrum.* **1993**, *64*, 1868−1873.
(42) Churnside, A. B.; Tung, R. C.; Killgore, J. P. Quantitative Contact Resonance Force Microscopy for Viscoelastic Measurement of Soft Materials at the Solid−Liquid Interface. *Langmuir* **2015**, *31*, 11143−11149.
(43) Sader, J. E.; Larson, I.; Mulvaney, P.; White, L. R. Method for the Calibration of Atomic Force Microscope Cantilevers. *Rev. Sci. Instrum.* **1995**, *66*, 3789−3798.
(44) Sader, J. E.; Chon, J. W. M.; Mulvaney, P. Calibration of Rectangular Atomic Force Microscope Cantilevers. *Rev. Sci. Instrum.* **1999**, *70*, 3967−3969.
(45) Killgore, J. P.; Yablon, D. G.; Tsou, A. H.; Gannepalli, A.; Yuya, P. A.; Turner, J. A.; Proksch, R.; Hurley, D. C. Viscoelastic Property Mapping with Contact Resonance Force Microscopy. *Langmuir* **2011**, *27*, 13983−13987.
(46) Yuya, P. A.; Hurley, D. C.; Turner, J. A. Contact-Resonance Atomic Force Microscopy for Viscoelasticity. *J. Appl. Phys.* **2008**, *104*, No. 074916.
(47) PERIODOGRAM, Y., PERIODOGRAM Graphics Commands.
(48) Ma, C.; Zhou, C.; Peng, J.; Chen, Y.; Arnold, W.; Chu, J. Thermal Noise in Contact Atomic Force Microscopy. *J. Appl. Phys.* **2021**, *129*, No. 234303.
(49) Stan, G.; King, S. W. Atomic Force Microscopy for Nanoscale Mechanical Property Characterization. *J. Vac. Sci. Technol., B: Nanotechnol. Microelectron.: Mater., Process., Meas., Phenom.* **2020**, *38*, No. 060801.
(50) Rabe, U.; Janser, K.; Arnold, W. Vibrations of Free and Surface-Coupled Atomic Force Microscope Cantilevers: Theory and experiment. *Rev. Sci. Instrum.* **1996**, *67*, 3281−3293.
(51) Efremov, Y. M.; Okajima, T.; Raman, A. Measuring Viscoelasticity of Soft Biological Samples Using Atomic Force Microscopy. *Soft Matter* **2020**, *16*, 64−81.
(52) Gonzalez-Martinez, J. F.; Kakar, E.; Erkselius, S.; Rehnberg, N.; Sotres, J. The Role of Cross-Linking in the Scratch Resistance of Organic Coatings: An Investigation Using Atomic Force Microscopy. *Wear* **2019**, *418*−*419*, 151−159.
(53) Rabe, U.; Amelio, S.; Kester, E.; Scherer, V.; Hirsekorn, S.; Arnold, W. Quantitative Determination of Contact Stiffness Using Atomic Force Acoustic Microscopy. *Ultrasonics* **2000**, *38*, 430−437.
(54) Yuya, P. A.; Hurley, D.; Turner, J. Relationship Between Q-factor and Sample Damping for Contact Resonance Atomic Force Microscope Measurement of Viscoelastic Properties. *J. Appl. Phys.* **2011**, *109*, No. 113528.
(55) Asif, S. A. S.; Wahl, K. J.; Colton, R. J. Nanoindentation and Contact Stiffness Measurement Using Force Modulation with a Capacitive Load-Displacement Transducer. *Rev. Sci. Instrum.* **1999**, *70*, 2408−2413.
(56) Valle-Delgado; Molina-Bolivar, J. J.; Galisteo-Gonzalez, F.; Gálvez-Ruiz, M. J.; Feilera, A.; Rutland, M. Interactions Between Bovine Serum Albumin Layers Adsorbed on Different Substrates Measured with An Atomic Force Microscope. *Phys. Chem. Chem. Phys.* **2004**, *6*, 1482−1486.
(57) Péterfi, Z.; Kocsis, B. Comparison of Blocking Agents for an ELISA for LPS. *J. Immunoassay* **2000**, *21*, 341−354.
(58) Bhavanandan, V. P.; Hegarty, J. Identification of the Mucin Core Protein By Cell-Free Translation of Messenger RNA from Bovine Submaxillary Glands. *J. Biol. Chem.* **1987**, *262*, 5913−5917.

https://doi.org/10.1021/acsomega.3c03740
ACS Omega 2023, 8, 32765−32774

(59) Scawen, M.; Allen, A. The Action of Proteolytic Enzymes On The Glycoprotein from Pig Gastric Mucus. *Biochem. J.* **1977**, *163*, 363−368.
(60) Bettelheim, F. A.; Block, A. Water Vapor Sorption of Bovine and Porcine Submaxillary Mucins. *Biochim. Biophys. Acta, Gen. Subj.* **1968**, *165*, 405−409.
(61) Hurley, D. C.; Turner, J. A. Humidity Effects on the Determination of Elastic Properties by Atomic Force Acoustic Microscopy. *J. Appl. Phys.* **2004**, *95*, 2403−2407.
(62) Hurley, D. C.; Kopycinska-Müller, M.; Julthongpiput, D.; Fasolka, M. J. Influence of Surface Energy and Relative Humidity on AFM Nanomechanical Contact Stiffness. *Appl. Surf. Sci.* **2006**, *253*, 1274−1281.
(63) Eslami, B.; Caputo, D. Effect of eigenmode frequency on loss tangent atomic force microscopy measurements. *Appl. Sci.* **2021**, *11*, 6813.
(64) Em-Udom, J.; Pisutha-Arnond, N. Investigation of Viscoelastic-Creep and Mechanical-Hysteresis Behaviors of Hydrostatically Stressed Crystal Using the Phase Field Crystal Method. *Adv. Math. Phys.* **2020**, *2020*, 1−20.
(65) Kestin, J.; Whitelaw, J. H. The Viscosity of Dry and Liquid Humid Air. *Int. J. Heat Mass Transfer* **1964**, *7*, 1245−1255.
(66) Dinelli, F.; Biswas, S. K.; Briggs, G. A. D.; Kolosov, O. V. Measurements of Stiff-Material Compliance on the Nanoscale Using Ultrasonic Force Microscopy. *Phys. Rev. B* **2000**, *61*, 13995.

https://doi.org/10.1021/acsomega.3c03740
ACS Omega 2023, 8, 32765−32774